Moving Towards L-Band NASA-ISRO SAR Mission (NISAR) Dense Time Series: Multi-Polarization Object-Based Wetland Classification in Yucatan Lake, Louisiana

Sarina Adeli[1], Bahram Salehi[1], Masoud Mahidanpari[2], Lindi J. Quackenbush[1], Bruce Chapman[3]

[1]Department of Environmental Resources Engineering, State University of New York College of Environmental Science and Forestry (ESF), Syracuse, New York, USA

[2]C-CORE and Department of Electrical Engineering, Memorial University of Newfoundland, St. John's, NL A1B 3X5, Canada

[3] NASA Jet Propulsion Laboratory, California Institute of Technology, Pasadena, CA 91109, USA

Corresponding author: Sarina Adeli (sadeli@esf.edu)

Key Points:

- High spatial resolution Earth Observation (EO) data and machine learning techniques have provided opportunities for preservation of wetlands.
- L-band simulated NISAR was captured with UAVSAR as a proxy for evaluating the planned NISAR for application of wetland monitoring.
- Using 84 polarimetric features and SVM and RF classifiers, the overall accuracies of 74.33% and 83.93% were obtained.

Abstract

Given the key role wetlands play in climate regulation and shoreline stabilization, identifying their spatial distribution is essential for the management, restoration, and protection of these invaluable ecosystems. The increasing availability of high spatial and temporal resolution optical and synthetic aperture radar (SAR) remote sensing data coupled with advanced machine learning techniques have provided an unprecedented opportunity for mapping complex wetlands ecosystems. A recent partnership between the National Aeronautics and Space Administration (NASA) and the Indian Space Research Organization (ISRO) resulted in design of the NASA-ISRO SAR (NISAR) mission. In this study, the capability of L-band simulated NISAR data for wetland mapping in Yucatan Lake, Louisiana is investigated using two object-based machine learning approaches: Support Vector Machine -(SVM) and Random Forest (RF). L-band Unmanned Aerial Vehicle SAR (UAVSAR) data is exploited as a proxy for NISAR data. Specifically, we evaluated the synergistic use of different polarimetric features for efficient delineation of wetland types, extracting 84 polarimetric features from more than 10 polarimetric decompositions. High spatial resolution National Agriculture Imagery Program imagery is applied for image segmentation using the mean-shift algorithm. Overall accuracies of 74.33% and 81.93% obtained by SVM and RF, respectively, demonstrate the great possibility of L-band prototype NISAR data for wetland mapping and monitoring. In addition, variable importance analysis using the Gini index for RF classifier suggests that H/A/ALPHA, Freeman-Durden, and Aghababaee features have the highest contribution to the overall accuracy.

Plain Language Summary

By illuminating the surface SAR signals can provide meaningful information on the shape, geometry, and roughness of the surface. In particular, polarimetric decompositions brings a measure of the relative contribution of backscatter from different scattering mechanism that can be used for wetland delineations, classification, and monitoring. Given the availability of various polarimetric decompositions, the selection of appropriate decomposition based on the application and SAR sensor configuration is crucial. In this study, we investigated the performance of various polarimetric decompositions for delineating wetlands classes over Yucatan Lake in Louisiana. The adopted machine learning classification workflow was applied to the L-band simulated NISAR data that is acquired by the UAVSAR platform to evaluate the performance of planned L-band NISAR data. Our investigations showed that H/A/ALPHA, Freeman-Durden, and Aghababaee features have the highest contribution to the overall accuracy.

1. Introduction

Wetlands are defined as the transitional zone between water and land. The soil in these natural infrastructures is covered with water either permanently or for portions of the year (e.g., growing season) (Gardner & Davidson, 2011). According to Tiner et al.(2015) between 3–8% of the Earth's land surface has been covered by wetlands (Tiner et al., 2015). Wetlands are highly productive and provide significant ecosystems services at regional and global scales (Bartsch et al., 2009), including facilitating water storage and purification, weather regulation, storm protection, flood mitigation, and shoreline stabilization (Mitsch et al., 2013). Moreover, the prolonged presence of water favors the growth of some endangered terrestrial and aquatic vegetation species (Dahl 2011). Due to the inherent wet conditions of these lands, they also are considered ideal regions for sequestering and storing atmospheric carbon (Bridgham et al. 2006). According to Bloom et al. (2010), wetlands also emit 20% to 25% of global carbon emission.

Despite the intrinsic importance of wetlands, they are being degraded due to man-made and natural threats. One of the main issues in recent years is transformation of wetlands into agricultural fields due to the demand for intensive farming (Jaramillo et al., 2018). Another triggering factor for the permanent loss of wetlands is over-exploitation of underground aquifers. (Dahl 2011) reported that the rate of declining marine and estuarine intertidal wetlands is 1.4 percent in USA between 2004 and 2009. That percentage would be equal to 84,100 acres (34,050 ha). In particular for coastal wetlands of Atlantic, Pacific, and Gulf of Mexico coasts the rate for wetland loss is 19,000 acres per year for 1922–1954 and 46,000 acres per year for 1954–1974 (Stedman & Dahl, 2004) . This extensive loss of wetlands may hinder future economic, tourism, and technological advances. Due to the severe wetland loss over large extents, wetland mapping and monitoring using remote sensing data have gained more attention in the remote sensing community in recent years (Brisco et al., 2015; Mitsch et al., 2013; Wohlfart et al., 2018).

Over the past two decades, remote sensing data has significantly facilitated wetland mapping and monitoring (Tiner et al., 2015; Tsyganskaya et al., 2018; Wohlfart et al., 2018). In particular, the ability of Synthetic Aperture Radar (SAR) sensors to collect data day and night in all-weather conditions makes this a highly valued data source for wetland monitoring. By providing medium to high spatial resolution imagery with a low revisit cycle, newer SAR datasets have proved to be a valuable tool for wetland monitoring (Wohlfart et al., 2018). Compared to other conventional methods for wetland monitoring such as optical imagery, SAR operates in longer wavelengths of the electromagnetic spectrum. This portion of the electromagnetic spectrum allows for deeper penetration of transmitted signals in vegetation cover, which enhances efficient delineation of different wetland classes. Moreover, sensitivity of the SAR signal to the roughness and dielectric properties of the surface, supports retrieval of information related to the shape, size, orientation, and moisture content of the target (Tsyganskaya et al., 2018).

SAR sensors operate at different frequencies including L (24 cm wavelength), C (5.66 cm wavelength) and, X (3 cm wavelength) bands. The wavelength in which the sensor operates is an influential factor in the penetration depth and signal attenuation. Due to the longer wavelength, L-band has deeper penetration depth and weaker attenuation through vegetation canopy compared to other frequencies, such as C-band (Hong & Wdowinski, 2014). This allows L-band to penetrate through dense wetland vegetation structure and reach the water surface. According to Ott et al. (1990), L-band also is more sensitive to the available moisture content in the vegetation cover. These characteristics have made L-band ideal for mapping the dense cover prevalent in herbaceous wetlands (Zhao et al., 2018). In a study conducted in the Amazonian basin, Hess et al. (2015) classified wetlands using L-band JERS-1 mosaics with 100-m resolution. They used dual season backscattering values for estimating the extent of wetland and inundation state and found relatively high producer's accuracy (better than 85%) for wetland extent (Hess et al., 2015). Several studies have also reported an increase in overall accuracy of wetlands classification by integrating different SAR frequency bands (Evans & Costa, 2013; Mahdianpari et al., 2017; Mohammadimanesh et al., 2018).

Another factor influencing SAR sensor capability is polarization. Given the sensitivity of SAR signal to different backscattering mechanisms, full-polarimetric SAR data can facilitate distinguishing similar wetlands classes (Brisco et al., 2015). Compared to single or dual polarimetric SAR sensor configurations, full-polarimetric systems preserve the phase between the sensor and target, which allows for decomposition of coherency and covariance matrices. To this end, researchers have developed several techniques to decompose polarimetric SAR images into different classes based on scattering signatures (Cloude & Pottier, 1996; Freeman & Durden,

1998a; Touzi, 2007). Polarimetric decompositions can categorize ground targets using three different main scattering mechanisms: odd/single bounce, even/double bounce, and volume scattering. In wetlands, odd/single bounce can be attributed to direct scattering from open water. An example of even/double bounce is the scattering between a tree trunk and open water, which is prevalent in flooded vegetation areas. Volume scattering in wetlands mostly occurs as multiple scattering in the dense canopy structure. Adeli et al. (2020) provide a comprehensive review of studies focused on wetland monitoring using SAR data.

A joint partnership between the National Aeronautics and Space Administration (NASA) and the Indian Space Research Organization (ISRO) has led to development of the spaceborne NASA-ISRO SAR (NISAR) program (Hoffman et al., 2015). NISAR will be instrumented with multi-polarimetric, dual-frequency L (24 cm wavelength) and S (10 cm wavelengths) band SARs for imaging the Earth. Notably, NISAR is equipped to receive twelve independents channels, enabling a 12-day global revisit cycle (Chuang et al., 2016). However, while the L-band SAR has the ability to collect all data while over land, the duty cycle of the S-band SAR is limited, and will be restricted to a planned subset of the Earth's surface. Considering both ascending and descending orbits, the mission plans to image at L-band the Earth's global land mass twice every 12 days. The full resolution of the L-band SAR data while in its most common operating mode will be 7 m across its entire 240 km swath width. A few studies have explored the use of simulated NISAR for environmental monitoring. For example, Yu and Saatchi (2016) predict that NISAR will be able to generate global biomass map in short time frame, given the deeper penetration depth of L-band and short revisit cycle (Yu and Saatchi 2016). Duncanson et al. (2020) used simulated NISAR, simulated ICESat-2 and GEDI data to estimate above-ground biomass in Sonoma County, California. Their achieved RMSE for each of the missions were 57%, 75%, and 89% for GEDI, NISAR, and ICESat-2 respectively. (Duncanson et al. 2020).

Albinet et al. (2019) report that NISAR will produce 40 PB of data per year. Although this will provide unprecedented global coverage in a short time frame, the high volume raises several challenging issues related to data processing in order to exploit, visualize, and discover the full potential of NISAR data. There are also issues that apply not only to use of the NISAR data, but are broader challenges in the classification of remote sensing data, e.g. the inherent complexity of land cover within wetlands and the limitation of training data. Fortunately, the development of advanced machine learning such as Random Forest (RF) and Support Vector Machines (SVM) and deep learning techniques such as Convolutional Neural Network (CNN) provides a significant contribution in terms of handling large-volume multi-temporal SAR data (Banks et al., 2019; Mahdianpari et al., 2017; Thanh Noi & Kappas, 2018). RF classifies an image using many decision trees that are trained based on subtle variations of the same training dataset, hence, the group of trees is less affected by overfitting compared to a single decision tree (Banks et al., 2019). SVM converts input data to a high-dimensional feature space and divides the feature space using optimal hyperplanes. SVM is more resistant to noise and unequal number of samples within each class (Mountrakis et al., 2011). According to Sheykhmousa et al. (2020) although deep learning techniques are powerful in reconstructing complex image patterns, they suffer from hidden layer effects that can result in interpretability issues. Moreover, unlike SVM and RF classifiers, deep learning techniques are more dependent on the presence of the high density and high-quality ground reference data. Another issue with deep learning techniques is their high computational complexity. Hence, RF and SVM are still attracting attention from the remote sensing community since they have provided efficient solutions with results that are competitive relative to the more complex deep learning techniques (Sheykhmousa & Mahdianpari, 2020).

The USA National Wetland Inventory (NWI) adopted the Cowardin system for generating wetland inventory maps within the USA which includes five major systems, 11 classes and, 28 subclasses. (Cowardin et al., 1979). The classes for this system are defined based on various factors including chemical, hydrological, and geomorphological attributes. NWI updated the national wetland inventory map of the USA in May 2016. One of the reasons behind this update was the demand for having surface waters and wetlands as polygons in a single geospatial dataset. This second NWI version included more detailed data of the wetlands and water bodies. There are also a range of studies in the literature that use the Cowardin classification scheme. For instance, Pistolesi et al. (2015) classified Hudson Highlands ecoregion wetlands in New York using the Cowardin classification system. They unified classes palustrine emergent, palustrine scrub/shrub, and palustrine forested as emergent, scrub/shrub, and forested wetlands, respectively. The class of open water includes palustrine aquatic bed, palustrine unconsolidated bottom, and palustrine unconsolidated shore based on the definition in Cowardin classification systems (Pistolesi et al., 2015). In another study, implemented in Minnesota, Corcoran et al. (2013) used a two-level RF classifier to classify wetlands in six major classes of forested uplands, open water, forested, scrub/shrub, and emergent wetlands. The classification was based on a modified version of Cowardin classification systems (Corcoran et al., 2013).

The fully polarimetric SAR data allows for the recreation of covariance and coherency matrices that can be led to attaining polarimetric decompositions elements. Hence the implementation of polarimetric decomposition pertains with separation of received signal to different scattering mechanism that are established to be advantageous for wetland separation analysis (Mohammadimanesh et al. 2019; Brisco et al. 2013; Koch et al. 2012). While the upcoming NISAR mission is expected to acquire SAR imagery in only dual-polarization (HH and HV) rather than full polarization for most of the Earth's entire land mass, NISAR does have the capability of acquiring fully polarimetric L-band SAR data, and an extended mission scenario could include collection of fully polarimetric data over more extended areas. Therefore, the primary objective of this study was to assess the ability of fully polarimetric L-band simulated NISAR data for delineating wetlands complex using two machine learning classifiers. In particular, this study aims to: (1) compare the efficiency of object-based SVM and RF techniques for classifying L-band prototype science products; (2) evaluate the capability of recent polarimetric decomposition techniques for classifying wetlands complex; (3) explore the relative importance of polarimetric features in RF models, and (4) test the impact of SVM parameter selection on overall accuracy. To this end, once the raw L-band simulated NISAR data are preprocessed, 84 polarimetric features from more than 10 polarimetric decompositions are extracted.

2. Study area, classification system and NISAR data

Most parts of northeastern Louisiana are covered by rivers, lakes, and forested areas. This study focuses on Yucatan Lake in an unincorporated community covered by inundated willows and Cyprus trees, and in some part by crops. The aquatic environment of this area contains several ponds. The lake lies 8.36 kilometers from Newellton and 16.10 kilometers from Saint Joseph in Tensas Parish in Tenses County. The extent of Yucatan Lake is estimated to be around 10 square kilometers. The elevation around the lake varies from 20 to 66 feet. From the climate perspective, the temperature in the area changes from 37° F in December to 93 Fahrenheit in July. The highest average monthly precipitation varies from 3.06 inches in September to 6.31 inches in January and

March (Yucatan Lake Topo Map in Tensas Parish, Louisiana). Figure 1 shows the geographic location of the study area (left) and the simulated NISAR scene (right).

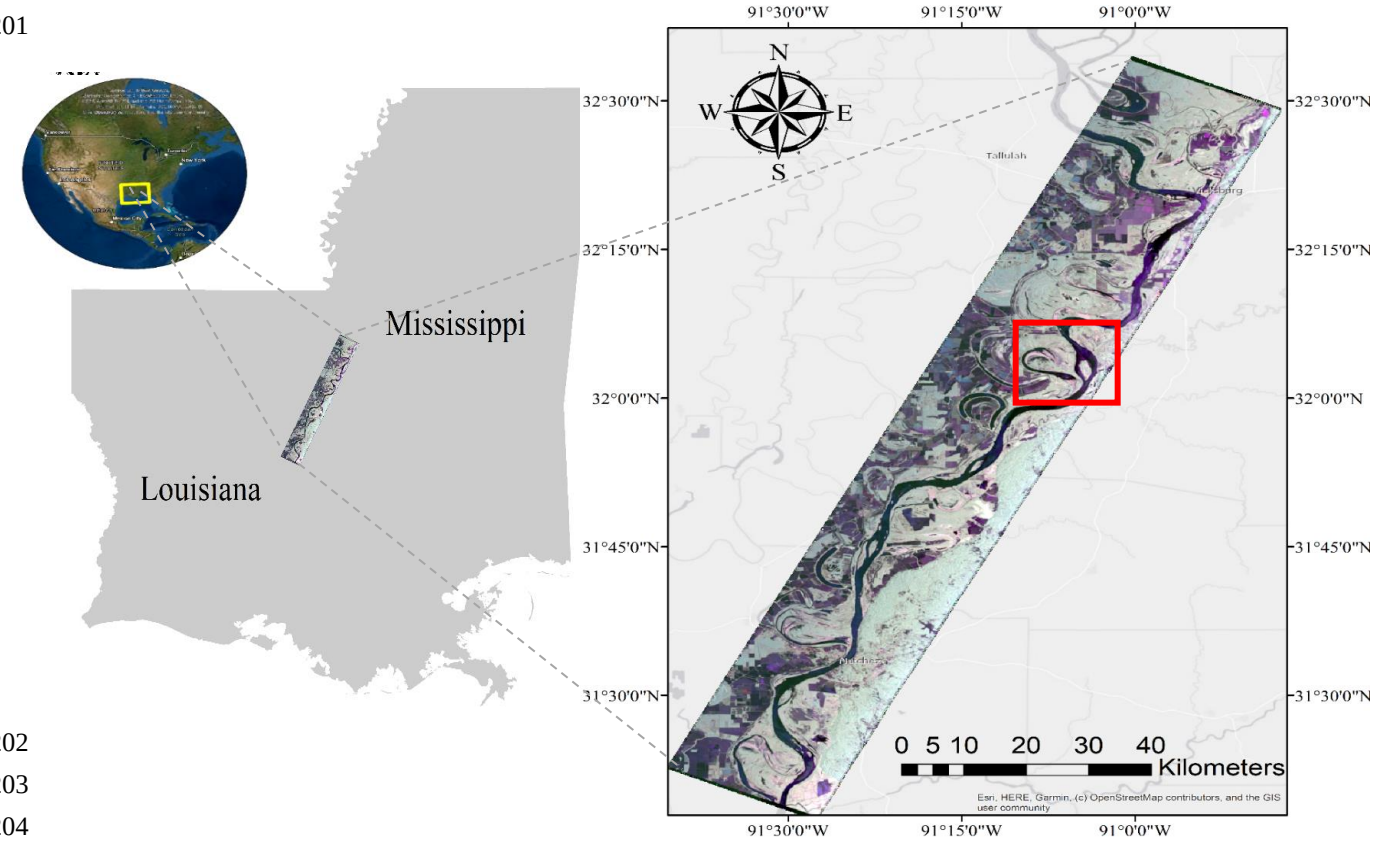

Figure 1. Left: Geographic location of the Yucatan Lake is shown by a red rectangle in the boundary between northeastern Louisiana and Mississippi. Right: The simulated NISAR image. The date of this image is 30 Septemer 2019, and it was acquired in the morning at 9:17am local time.

2.1. UAVSAR and Simulated NISAR data

Full polarimetric L-band UAVSAR data was collected over the Yucatan lake area 13 times between June and October, 2019. The UAVSAR instrument flies on a NASA Gulfstream 3 jet, and is equipped with a multi-polarimetry SAR sensor operating at L-band (23.5 cm wavelength). The collected data is part of NISAR UAVSAR AM/PM campaign to collect L-band SAR data with a similar observation cadence as NISAR for algorithm development and calibration (Chapman et al. 2019). The data were specially processed to mimic NISAR noise and resolution characteristics by the UAVSAR project. In particular, L-band simulated NISAR imitates the polarizations, incidence angles and signal-to-noise level of upcoming real NISAR data configurations (Huang et al. 2021). The duration of this data take was approximately 12 minutes. The UAVSAR data sampling was reduced from the standard UAVSAR slant range pixels of 0.8 x1.7 m to 10x10 m on the ground, corresponding to the smallest possible NISAR pixel spacing being considered for its products. The UAVSAR swath width is 16 km, but since incidence angles are limited on NISAR

to 34° in near range and 48° in far range (Kraatz et al., 2020), the corresponding incidence angle restricted swath width for UAVSAR is about 5 km. Compared to planned NISAR performance, UAVSAR has a higher signal to noise ratio and much higher resolution. Hence, the NASA Jet Propulsion Laboratory's (JPL) reduced the resolution and added Gaussian noise to the UAVSAR data. Moreover, the simulated NISAR data is coregistered on same grids. This characteristic eases time-series analysis applications. Further, given the need for radiometric terrain corrected backscatter, the simulated NISAR products comes with a radiometric terrain correction (RTC) calibration file (Simulated NISAR Products 2020). For comparing the characteristics of simulated NISAR and real NISAR data, the characteristics of real NISAR data is provided in Table 1.

Table 1. Characteristics of the upcoming NISAR mission.

Characteristics	Descriptions
Operating frequency	L-band (24 cm wavelength) and S-band (10 cm wavelength)
Full Spatial resolution	7 m in azimuth over a swath width of ~242 km, variable in range depending on mode
Repeat orbit	12-day
Altitude	740 km
Polarization	L: Single-pol through quad-pol, including compact-pol and split-band dual-pol
Incidence Angle Range	34°–48°
Range resolution	3–10 m
Azimuth resolution	7 m

2.2. Training and test reference data description

The NWI map of the area reveals that the area is covered by lakes, river, freshwater ponds, forested scrub/shrub wetlands and, emergent wetlands. National Agriculture Imagery Program (NAIP) is responsible for acquiring aerial imagery (with 1 meter resolution) during agricultural growing season within USA (USDA-FSA-APFO Aerial Photography Field Office, 2015). In this study a mosaic of NAIP imagery over our study site was overlaid onto the NWI wetland map of the Louisiana state. The series of NAIP imagery was captured in 2019 in leaf- on condition season. The wetland map of Louisiana state was downloaded from NWI website in the format of .shp. Once the .shp file loaded in the ArcMap, the attribute was set to the wetland type on its unique values. The scene of the simulated NISAR imagery was also overlaid to assure the consistency of borders and coregistration among these three layers. Next, the type of dominant wetland in each region was determined using NWI map. Ultimately, the borders of digitized reference polygons was drawn by relying on the NAIP imageries on leaf-on season.

The classes that were assigned to digitized polygons followed a modified version of the Cowardin classification scheme. This study used six major classes: emergent, forested scrub/shrub wetlands, open water, freshwater pond, forested upland and cultivated/planted land. The class of forested scrub/shrub wetland defined as forested swamp or wetland shrub bog or wetland that parallels to palustrine forested and/or palustrine shrub in the Cowardin system. Table 2 provides a summary of the classes considered, their abbreviations, and brief descriptions of each class. The total reference data employed were divided with 70% used as training data for the classifier and the rest used for testing.

Table 2. Description of wetland classes used in this study and their corresponding NWI and Cowardin class names and code.

NWI class name	Cowardin class code	Cowardin Class	Description	Classes Used
Freshwater-Forested and Shrub wetland	PFO, PSS	Palustrine forested or Palustrine shrub	Forested swamp or wetland shrub bog	Forested scrub/ shrub wetland
Freshwater Emergent wetland	PEM	Palustrine emergent	Herbaceous marsh, fen, swale and wet meadow	Emergent Wetland
Freshwater pond	PUB, PAB	Palustrine unconsolidated bottom, Palustrine aquatic bed	Pond	Freshwater Pond
Riverine	R	Riverine wetland and Deepwater	River or stream channel	Open Water
Lakes	L	Lacustrine wetland and Deepwater	Lake or reservoir basin	
Uplands	UPL	_____	_____	Planted/cultivated lands and Forested Uplands

3. Methods

3.1. Georeferencing and speckle filter

L-band simulated NISAR data was geo-referenced based NAD1983 UTM zone 15. After the simulated NISAR images were georeferenced, we implemented a speckle reduction filter. An enhanced Lee filter with 5×5 window size was applied for reducing speckle (Jong-Sen Lee et al., 2009). Unlike non-adaptive speckle filters, the enhanced Lee filter is adaptive, meaning it does not smooth the entire image to the same degree. Depending on the spatial location of each pixel, the enhanced Lee adaptive filter preserves edges, shapes, and texture of the image by lowering the standard deviation of neighboring pixels. The ultimate result is an image with reduced noise but has edges and image quality preserved (Choi & Jeong, 2019; Jong-Sen Lee et al., 2009).

3.2. Polarimetric decomposition

The main goal of polarimetric decomposition is to separate the backscattering signal based on different scattering mechanisms. Depending on various sensor and target factors, including the roughness and dielectric properties of the surface, different backscattering mechanisms are expected from a specific land cover (Furtado et al., 2016). Generally, there are two types of decompositions: coherent and incoherent. While coherent decomposition is impractical for separating different natural targets due to a high degree of noise, incoherent decomposition is more applicable. Table 3 shows a number of different incoherent decomposition techniques and their corresponding polarimetric features.

Table 3. Incoherent decomposition techniques and corresponding polarimetric features.

Decompositions	Extracted Polarimetric Features
Pauli	Pauli_a, Pauli_b, Pauli_c
Krogager	Krogager_Ks, Krogager_Kd, Krogager_Kh
Freeman-Durden	Freeman_Vol, Freeman_Odd, Freeman_Dbl
H/A/Alpha	Entropy, Anisotropy, Shannon Entropy, H/A/A, T11, H/A/A_T22, H/A/A_T33, DERD, Polarization Asymmetry, Polarization Fraction, SERD, Radar Vegetation Index, Anisotropy12, Pedestal Height, Alpha, Anisotropy_Lueneburg, Pseudo Probabilities (p1, p2, p3), Lambda
Yamaguchi	Yamaguchi_Vol, Yamaguchi_Odd, Yamaguchi_Dbl, Yamaguchi_Hlx
An_Yang	An_Yang Vol, An_Yang_Odd, An_Yang_Dbl An_Yang_Hlx
Touzi	TSVM_alpha_s, TSVM_alpha_s1, TSVM_alpha_s2, TSVM_alpha_s3, TSVM_tau_m, TSVM_tau_m1 TSVM_tau_m2, TSVM_phi_s2, TSVM_psi1 TSVM_psi, TSVM_tau_m3, TSVM_phi_s3 TSVM_psi2, TSVM_phi_s1, TSVM_phi_s, TSVM_psi3
Singh	Singh _Vol, Singh _Odd, Singh _Dbl, Singh _Hlx
Huynen	Huynen_T11, Huynen_T22, Huynen_T33
VanZyl	VanZyl_Vol, VanZyl_Odd, VanZyl_Dbl
Aghababaee	Aghababaee_Alphap_mean, Aghababaee_Alphap_SM1, Aghababaee_Alphap_SM2, Aghababaee_Alphap_SM3, Aghababaee_M_SM1, Aghababaee_M_SM2, Aghababaee_M_SM3, Aghababaee_Orientation_max_mean, Aghababaee_Orientation_max_SM1, Aghababaee_Orientation_max_SM2,

Aghababaee_Orientation_max_SM3, Aghababaee_Tawp_mean, Aghababaee_Tawp_SM1, Aghababaee_Tawp_SM2, Aghababaee_Tawp_SM3

As mentioned previously, polarimetric decomposition techniques can facilitate the physical interpretation of land cover types by decomposing the received signal into the scattering responses. The results of 11 decompositions applied to L-band UAVSAR data- as a prototype for planned NISAR- of the study area are illustrated in Figure 2(a)–(k). NAIP imagery of the study area is also presented to provide a visual assessment of the study site (Figure 2(l)). Color coding of the decomposition images in Figure 2 is as follows: odd-scattering is blue, even-scattering is red, and volume scattering as green. Double-bounce scattering can be attributed to the return signal from ground trunks or emergent wetlands. Most of the dark areas correspond to open water since the backscattering signal from calm water is usually weak (Qi et al., 2012).

Pauli is based on the decomposition of the scattering matrix in the form of complex addition of the Pauli basis. Pauli decomposition uses the scattering matrix elements to produce three elements: odd-scattering, even-scattering, and volume scattering (Cloude & Pottier, 1996) Figure 2(a). Krogager decomposes the scattering matrix in form of factorization of a sphere, a diplane, and a helix. For interpretation of the Krogager decomposition, the phase values are usually ignored and three parameters that correspond to the weight coefficient of sphere, diplane and, helix are considered. Although Krogager is a coherent decomposition and generally is more applicable for man-made structures such as urban areas, it has provided a well-balanced interpretation of the targets such as vegetation and water area in Figure 2(b). The combination of powers scattered by a sphere, diplane- and the helix-like component of the Krogager generated the color code for visualization (Krogager, 1990).

The three component Freeman-Durden decomposition has proven to have a good ability to discriminate between flooded and non-flooded forests especially in tropical regions. The ability of Freeman-Durden in discriminating different vegetation covers can be attributed to the scattering model of this decomposition, which contains randomly oriented dipoles and double bounce scatterer that can result from a corner-reflector (L-shape target) target. This decomposition categorizes the scene by extracting the different scattering mechanisms from the covariance matrix (Freeman & Durden, 1998b). The decomposition results in Figure 2(c) show that emergent wetlands and urban areas are identified using double-bounce. We expect that open water, freshwater pond areas, and some part of cultivated/planted land will be detected using the odd-bounce mechanism and finally, forested scrub-shrub wetlands will be detected by volume scattering. The fourth decomposition implemented (Figure 2(d)) is H/A/ALPHA, so named for its three main features: Entropy (H), Anisotropy (A), and Alpha angle. Entropy represents the heterogeneity of a single scatter; the higher the entropy the larger the number of detected scattering mechanisms and low entropy meaning one scattering mechanism is detected. Anisotropy is a normalized ratio of eigenvalues and is defined as the dominancy of second scattering mechanisms. The last parameter is alpha, which is an angle that indicates the type of dominant backscattering mechanisms. A zero alpha angle illustrates that the surface scattering mechanism is prevailing,

where 45° and 90° incidence angles represent the dominance of double-bounce and volume scattering (Cloude & Pottier, 1997).

Yamaguchi decomposition extends Freeman-Durden decomposition by adding an element of helix scattering, which helps to distinguish co-pol and cross-pol ratios. The presence of helix scattering makes this decomposition perform better in urban areas (Yamaguchi et al., 2005), but the visualization of the decomposition is quite similar to the Freeman-Durden (Figure 2(e)). An&Yang decomposition is similar to the Yamaguchi decomposition in terms of decomposition features (Figure 2(f)) (Wang et al., 2020).

Touzi decomposition uses eigenvalue and eigenvector decomposition similar to H/A/ALPHA, but employs a roll-invariant coherent scattering model for decomposing eigenvectors of the coherency matrix. The parameter that is useful for vegetation structure mapping is the phase of symmetric scattering (Touzi, 2007). Although the Touzi decomposition image seems to be noisy (Figure 2(g)), Touzi (2010) found it to be a powerful decomposition approach for delineating different wetlands types. Touzi decomposition produces 15 different polarimetric features including the symmetric scattering-type magnitude, phase, and target helicity. Target helicity generated from this decomposition is better than H/A/ALPHA for forest characterization. The other component of this decomposition that can discriminate different herbaceous wetlands is the phase. Despite the efficiency of Touzi for wetland monitoring, the optimal integration of its features, including dominant, medium, and low single scatterings, is still debatable. The coherency matrix can also be decomposed into four different elements to create Singh decomposition (Singh et al., 2013). This decomposition allows for full utilization of polarimetric decomposition, due to its ability to distinguish the difference between the dihedral and dipole scattering in volume scattering. This decomposition is also better in identifying urban areas due to its sensitivity to HV polarization (Figure 2(h)).

Hyunen decomposes the coherency matrix into three different scattering mechanisms which are three eigen value of coherency matrix (Huynen, 1970). Although a theoretically powerful technique, there are major drawbacks of this decomposition and Li and Zhang (2016) found this decomposition provided little insight into the physics of scattering. Irregularity and asymmetry of the scattering elements, and instability are other drawbacks of this decomposition. However, Li & Zhang (2016) introduced a unified and improved version of this decomposition that has less irregularity and asymmetry (Figure 2(i)). Van Zyl is a decomposition of the nonnegative eigenvalue of the covariance matrix (Zyl, 1993). To estimate all scattering component of the polarimetric data, this decomposition combines the eigenvector decomposition of the covariance matrix to produce three components of odd, double, and volume scatterings (Figure 2(j)).

Similar to Freeman-Durden, Aghababaee decomposition is a model-based decomposition that employs multi-polarimetric SAR data as the sum of Kronecker products (SKP; Aghababaee & Sahebi, 2018). Aghababaee decomposition decomposes the target to direct, double-bounce, and random-volume scattering mechanisms. In particular, it can detect multiple scatterers in forested areas by using the SKPs of the covariance matrix. The results of Aghababaee decomposition seems a little noisy. The interesting thing about the RGB color code of this decomposition is that the open water has different colors in the Yucatan lake area and the river part (Figure 2(k)). Based on our knowledge from the area, this decomposition has weakness in discriminating different herbaceous

wetlands. However, this figure only shows one of the combinations of the three features that presumably has better visualization of the area.

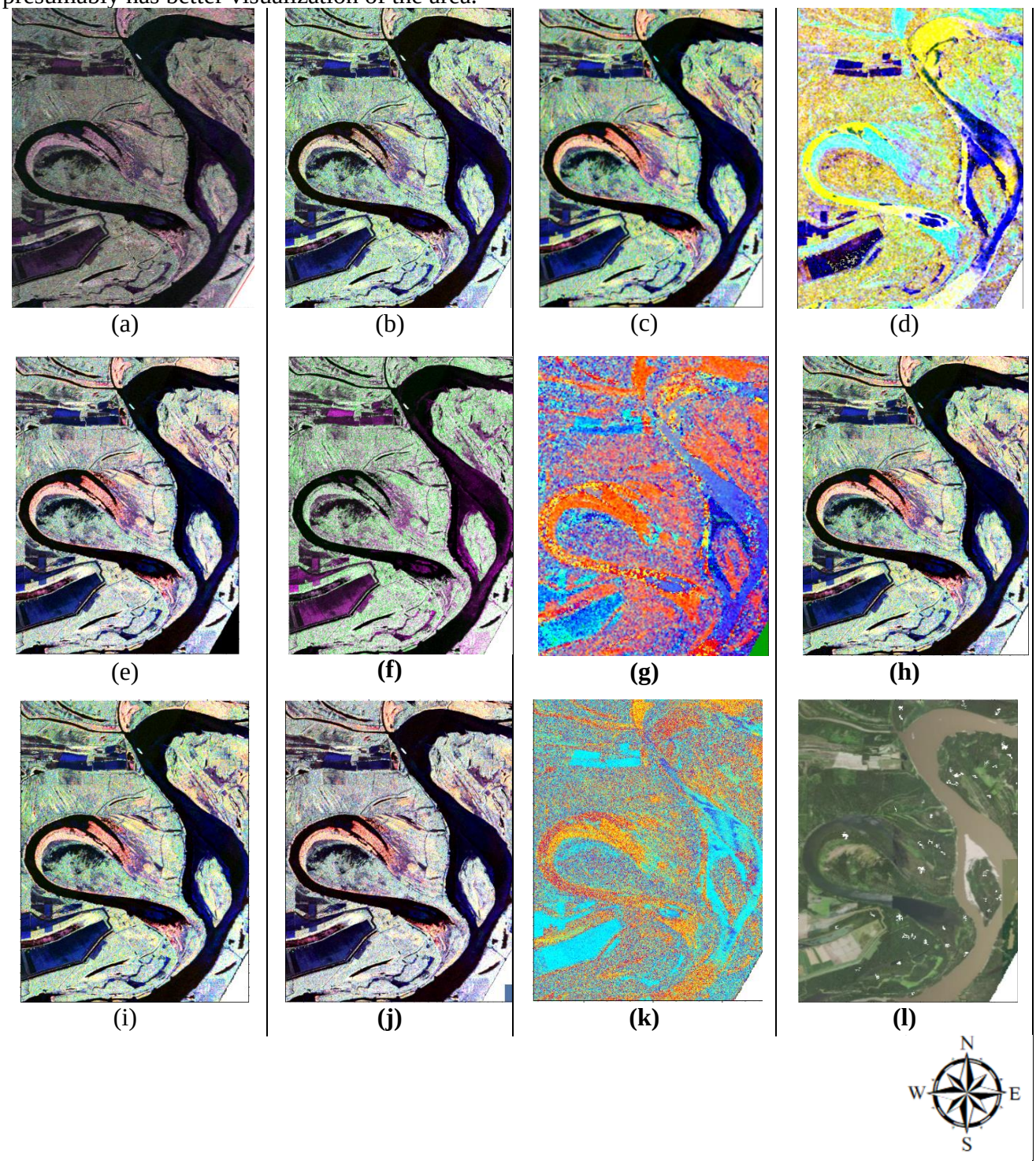

Figure 2. Implemented decompositions: (a) Pauli, (b) Krogager, (c) Freeman-Durden, (d) H/A/Alpha, (e) Yamaguchi, (f) An_Yang, (g) Touzi, (h) Singh, (i) Huynen (j): VanZyl, (k) Aghababaee; (l) normal color NAIP image of the study area shown in figure 1. The date of

UAVSAR imagery is 30 Septemer 2019, and it was acquired in the morning at 9:17am local time.

3.3. Object-based machine learning classifiers

This study implemented two object-based machine-learning algorithms (SVM and RF) to perform object-based classification of the simulated NISAR imagery. Object-based image analysis (OBIA) clusters pixels in order to create a segmented image that contains a grouped vector and defined geometry. The segmentation integrates contextual and spectral information to consider geographic information, color, and shape of each ground feature. As a result, the created objects bear more resemblance to real world features than pixel-based classifiers. Additionally, the salt and pepper noise that exists in the pixel-based image classification is eliminated in OBIA classifiers (Frohn et al., 2011; Salehi et al., 2018).

SVM defines decision boundaries called hyperplanes to separate different classes. The iterative learning process of SVM occurs by searching for an optimal hyperplane decision boundary to minimize misclassification (Zhu & Blumberg, 2002). Unlike conventional classification techniques (e.g. maximum likelihood) that assume normal distribution of training data, SVM is a non-parametric classification technique that holds no initial assumption about training data distribution (Mountrakis et al., 2011). Another appealing characteristic of SVM for geospatial data analysis is its capability to train and minimize the classification error using a small number of training samples. However, the choice of SVM kernel and parameters is not yet defined (Martins et al., 2016), hence in this paper, two parameters of C and gamma for the Radial Basis Function (RBF) kernel were examined.

RF classifiers use an integration of tree predictors in which each tree uses values from independently sampled random vectors (Pal 2005) RF is an attractive approach because it is also independent of assumptions about the normality of input data (Tian et al., 2016) and as the trees grow, best splits of a random subset of input features are chosen, which reduces correlation between separate trees. Another advantage of RF is that fewer variables need to be set for training the classifier. The number of trees trained in the RF classifier for this study was 200 and the number of seeds was equal to the square root of the number of samples (Mahdianpari et al. 2017).

Variable importance measures the prediction strength of each variable generated by each tree and can be considered as a post accuracy assessment for RF classifiers. The relative importance of each feature can be obtained using variable importance analysis (Rodriguez-Galiano et al., 2012). Two methods are common for variable importance analysis: permutation importance or mean decrease accuracy (MDA), which is based on out-of-box (OOB) error, and Gini importance or mean decrease impurity (MDI) (Millard & Richardson, 2015). In MDA, the average of each tree accuracies sort in decreasing order as a result of permutation. In this study, we used the MDI procedure for variable importance analysis since we aimed at testing the consistency our results with other investigations (Amani et al. 2018). MDI measures the importance of each feature in terms of the total number of samples divided by the number of tree splits. After calculating the Gini index for each of the polarimetric features, they were sort in decreasing order.

The flowchart of the classification is shown in Figure 3. 84 polarimetric features were extracted from the L-band simulated NISAR preprocessed data and stacked into one single vector. The object-based mean-shift segmentation was implemented using red, green, blue, and near infrared (NIR) bands of NAIP imagery (Tao, Jin, and Zhang 2007). The computational complexity of this approach is low and it can provide near real-time image segmentation. In the next step, the optimized parameters for achieving the highest accuracy of the SVM classifier were evaluated. Once the classifiers were trained, the stacked vector containing polarimetric features was imported into SVM and RF classifiers. The accuracy assessment of the classification results implemented using the validation samples in form of a confusion matrix. Ultimately, the variable importance analysis of the RF classifier was performed.

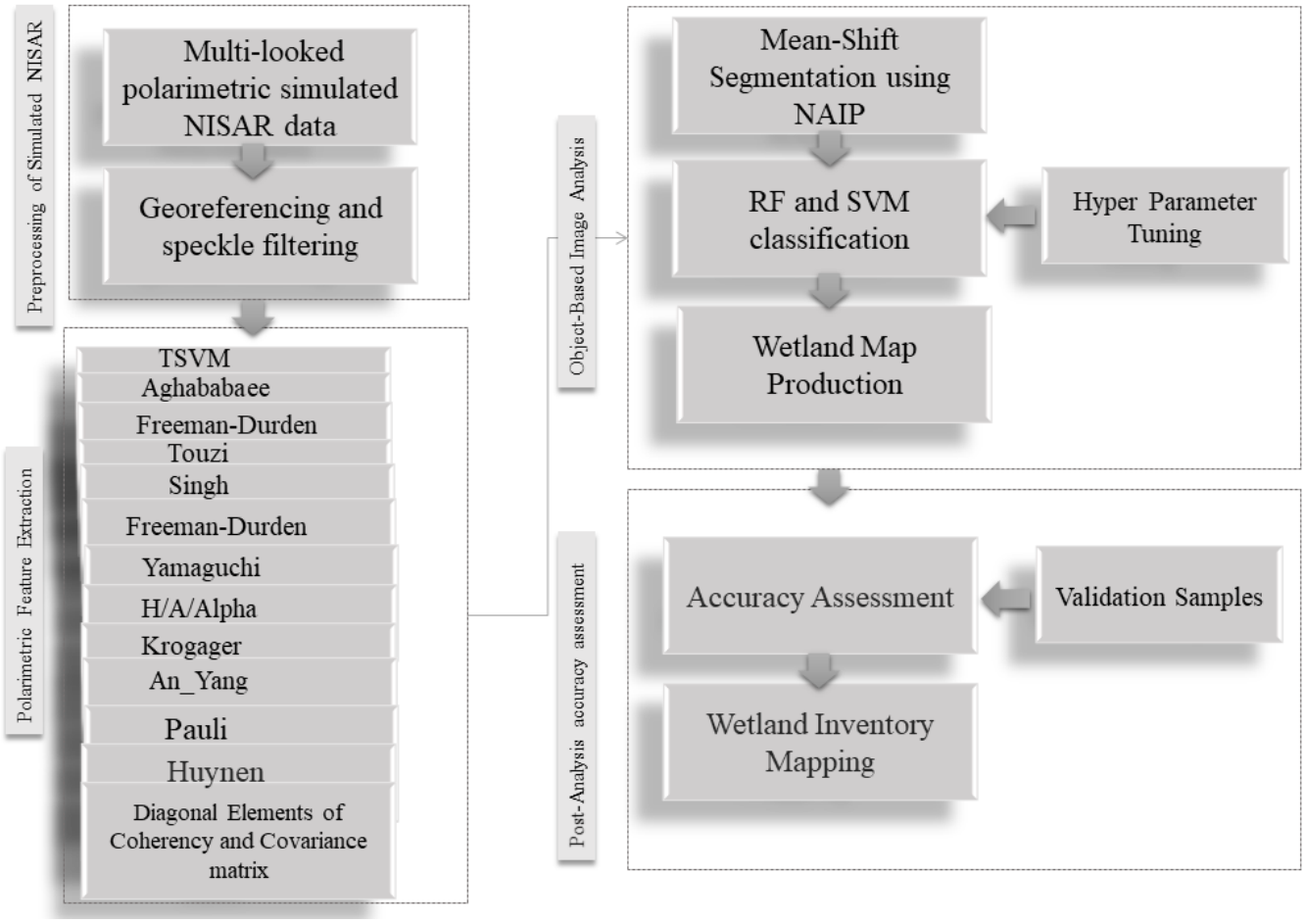

Figure 3. Flowchart of classification framework.

4. Results and Discussion

Thematic classification maps produced from the SVM and RF classifiers are shown in Figure (4) with six classes: open water, freshwater pond, forested scrub/shrub, forested upland, emergent wetland, and cultivated/planted land. An initial visual assessment of thematic maps suggests that forested scrub/shrub wetlands are dominant in the study area. Moreover, the RF classifier is better

in discriminating between forested upland and forested scrub/shrub wetland in the northeast of the study area. Emergent wetlands around Yucatan Lake are predominantly classified as forested scrub/shrub wetland rather than an emergent wetland. Moreover, the result of the RF classifier shows better discrimination between the freshwater pond and the Open water area.

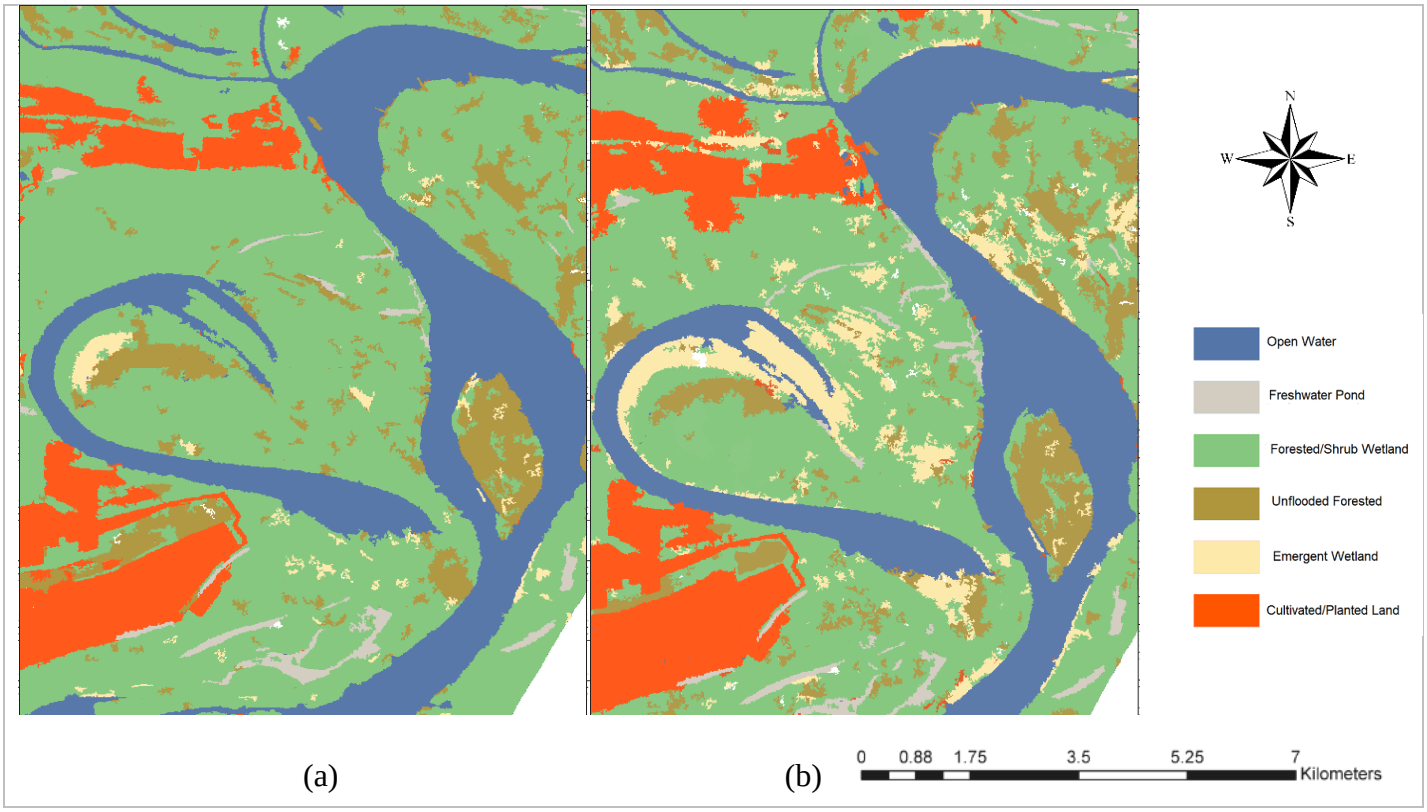

Figure 4. Object-based classification results: (a) SVM map; (b) RF map for the study area shown in figure 1.

4.1. Post analysis accuracy assessment

Selecting the parameters of the SVM kernel can considerably affect the overall classification accuracy. Hence, the optimal selection of a different combination of C and Gamma was examined. The resultant overall accuracy for different combinations of parameters are shown in the form of a heatmap in Figure 5. As can be seen, Gamma values higher than 10 and C values lower than 0.01 are better to be avoided in the classification, as they do not result in meaningful results. Overall, the combination of gamma values in the range of 0.001 to 10 and C values in the range of 0.1 to 1000 produced the results with accepted overall accuracies. Among the various tested combination of gamma and C, gamma equal to 0.1 and C equal to 10 provided the highest overall accuracy in our study.

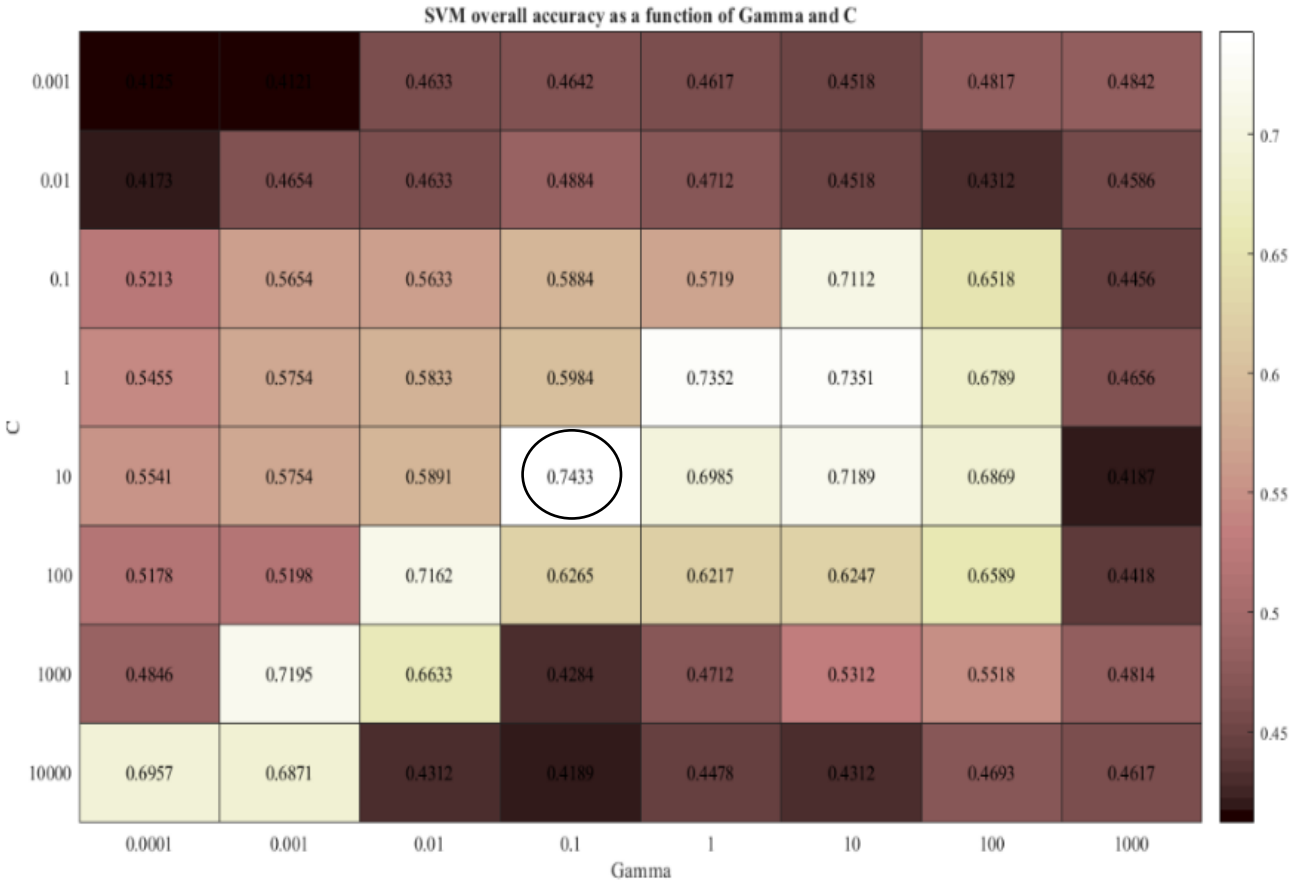

Figure 5. Variation in SVM overall accuracy based on different values of Gamma and C in the RBF kernel.

To provide quantitative assessment of the classification results, confusion matrices were calculated for both SVM and RF classifiers (Figure 6). The diagonal elements represent the producer's accuracy for each class. Overall accuracies of 74.33% and 81.93% were obtained for SVM and RF, respectively. The non-diagonal elements show the confusion between different classes. The non-diagonal elements corresponding to herbaceous vegetation for both classifiers in the confusion matrix are more noticeable compared to the non-vegetated area such as open water and cultivated/planted land. To elaborate, the non-wetland classes have higher accuracies which can be considered as a low commission and omission error. Theoretically, we expected to observe higher accuracies with increasing the reference data. Hence, the higher accuracy of non-wetland classes can be attributed to the larger availability of train data in the non-wetland classes. Potentially, due to the high similarity of backscattering signature between forested/shrub wetland and emergent wetland the confusion error for these two classes is higher for both classifiers. The confusion between the open-water and freshwater pond seen is likely due to the similarities of these two classes in SAR imagery. Notably, the confusion between the emergent wetland and forested scrub/shrub wetlands is higher in the SVM classifier compared to the RF classifier. The

other confusion is between the cultivated planted land and the open-water. This similarity can be attributed to the presence of odd-bounce scattering in both classes (Chen et al. 2014). Another confusion is between forested scrub-shrub wetland and cultivated/planted class that can suggest the presence of double-bounce in both classes. Ultimately, the confusion between the emergent wetland and forested/scrub shrub wetland is present in both classifiers which also is consistent with the result of Pistolesi et al. (2015).

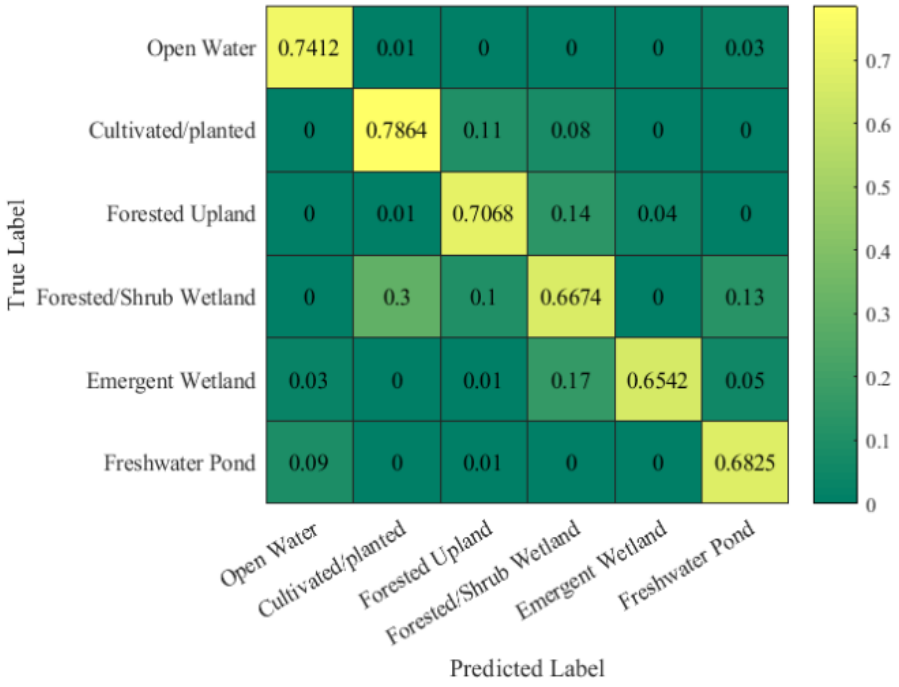

(a)

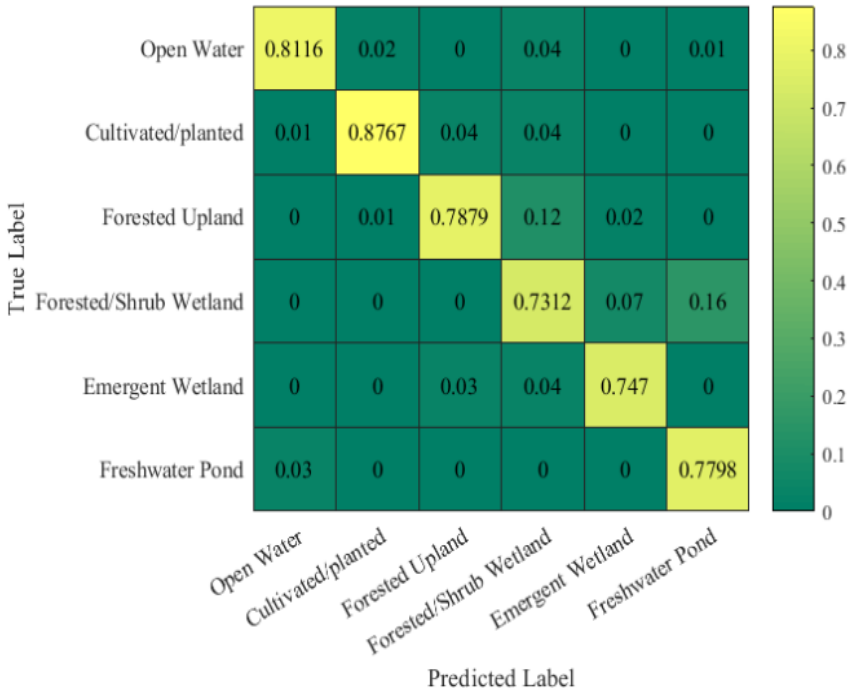

(b)

Figure 6. Confusion matrices of classification results: (a) SVM confusion matrix; (b) RF confusion matrix.

The relative importance of each polarimetric feature for the RF classifier was assessed using the Gini index. Figure 7 shows 84 polarimetric features sorted in decreasing order of importance, some of the H/A/ALPHA and Aghababaee features dominating in the highest levels. As shown in the figure, the first five of the polarimetric features have a high impact on the overall accuracy. After the fifteenth feature, the importance of polarimetric features decreases with a gradual slope. Hence, for future studies presenting the first fifteenth important features can be sufficient since including the rest of the features would not bring significant enhancement in the accuracy. Moreover, many polarimetric features correlate with each other, meaning they do not produce distinctive and meaningful results. The top parameters are all parameters that would be useful in identifying forest volume scattering. Most of the non-open water area here is in fact forested. It is far down before it hits a double bounce parameter, which should be an indicator of inundation in a forested area. These features are preferred to be eliminated from evaluations since they increase the processing time significantly. Ultimately, the one challenging issue that still needs to be resolved is the influence of the combination of polarimetric features on each other. For instance, the performance of Freeman-Durden features can vary in the presence of TSVM features (Amani et al. 2018).

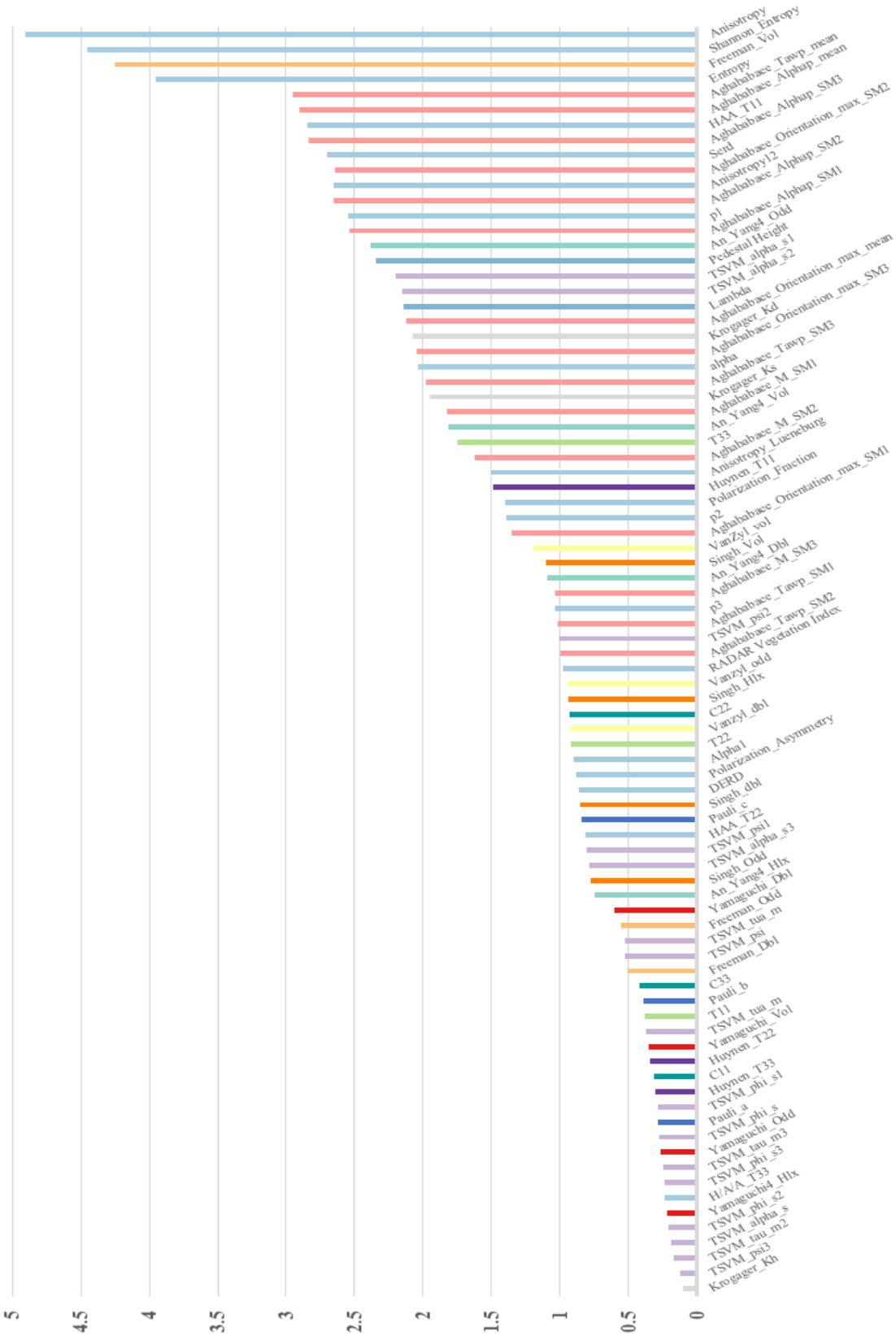

Figure 5. Variable importance analysis of object-based RF classifier.

5. Conclusions

Efficient extraction of information from geospatial datasets can facilitate management of complex wetland environments. As we move forward, more diverse data of higher quality are being acquired with satellite in sub-weekly basis. In this study, we used object-based SVM and RF classifications to classify L-band UAVSAR data, as a proxy for planned NISAR imagery, using 84 polarimetric features and achieved overall accuracy of 74.33% and 81.93%, respectively. The choice of parameters of RBF kernel was the influential factor in the SVM's overall accuracy. The confusion matrix of SVM demonstrates that SVM is a powerful classifier for delineating different upland classes. Likewise, the confusion matrix of RF classifier shows the superior ability of the RF classifier to distinguish between emergent wetland and forested scrub/shrub. It also explains the higher accuracy of RF classifier. Moreover, variable importance analysis of RF classifier demonstrated that among 11 different polarimetric decompositions H/A/ALPHA, Freeman-Durden, and Aghababaee have superior ability for discriminating different wetlands types. As expected, among different land-cover classes non-wetland classes including planted/cultivated land and open water had higher accuracies in both classifiers. The used imagery for this study was acquired in low flood date that means with the least contribution of double bounce scattering. For further studies, the inclusion of high flood imagery may increase the overall accuracies. Ultimately, this study confirmed the ability of simulated NISAR configuration for the discrimination of wetland classes using object-based machine learning classifiers.

The implemented ML classification scheme shall provide some initial insight on the application of L-band multi-polarization NISAR for wetland mapping and monitoring. The L-band NISAR data is planned to acquire data in dense time series, denser than Sentinel-1, with a global coverage. Large aperture reflectors and real time digital beamforming expected to bring a significant improvement in SAR capability for biomass remote sensing and solid earth surface observations. Ultimately, an accurate and meaningful wetland maps may leverage multi-frequency and multi-polarization satellite data with higher temporal resolution such as planned NISAR.

6. Acknowledgement

This research was partially carried out at the Jet Propulsion Laboratory, California Institute of Technology, under a contract with the National Aeronautics and Space Administration (80NM0018D0004).

The data used in this study is available online at https://uavsar.jpl.nasa.gov/cgi-bin/data.pl

7. References

Adeli, S., Salehi, B., Mahdianpari, M., Quackenbush, L. J., Brisco, B., Tamiminia, H., & Shaw, S. (2020). Wetland Monitoring Using SAR Data: A Meta-Analysis and Comprehensive Review. *Remote Sensing*, *12*(14), 2190. https://doi.org/10.3390/rs12142190

Aghababaee, H., & Sahebi, M. R. (2018). Model-Based Target Scattering Decomposition of Polarimetric SAR Tomography. *IEEE Transactions on Geoscience and Remote Sensing*, *56*(2), 972–983. https://doi.org/10.1109/TGRS.2017.2757062

Amani, M., Salehi, B., Mahdavi, S., Brisco, B., & Shehata, M. (2018). A Multiple Classifier System to improve mapping complex land covers: A case study of wetland classification using SAR data in Newfoundland, Canada. *International Journal of Remote Sensing*, *39*(21), 7370–7383. https://doi.org/10.1080/01431161.2018.1468117

Albinet, C., Whitehurst, A. S., Jewell, L. A., Bugbee, K., Laur, H., Murphy, K. J., Frommknecht, B., Scipal, K., Costa, G., Jai, B., Ramachandran, R., Lavalle, M., & Duncanson, L. (2019). A Joint ESA-NASA Multi-mission Algorithm and Analysis Platform (MAAP) for Biomass, NISAR, and GEDI. *Surveys in Geophysics*, *40*(4), 1017–1027. https://doi.org/10.1007/s10712-019-09541-z

Banks, S., White, L., Behnamian, A., Chen, Z., Montpetit, B., Brisco, B., Pasher, J., & Duffe, J. (2019). Wetland Classification with Multi-Angle/Temporal SAR Using Random Forests. *Remote Sensing*, *11*(6), 670. https://doi.org/10.3390/rs11060670

Bartsch, A., Wagner, W., Scipal, K., Pathe, C., Sabel, D., & Wolski, P. (2009). Global monitoring of wetlands – the value of ENVISAT ASAR Global mode. *Journal of Environmental Management*, *90*(7), 2226–2233. https://doi.org/10.1016/j.jenvman.2007.06.023

Bloom, A. A., Palmer, P. I., Fraser, A., Reay, D. S., & Frankenberg, C. (2010). Large-scale controls of methanogenesis inferred from methane and gravity spaceborne data. *Science (New York, N.Y.)*, *327*(5963), 322–325. https://doi.org/10.1126/science.1175176

Brisco, B., Murnaghan, K., Wdowinski, S., & Hong, S.-H. (2015). Evaluation of RADARSAT-2 Acquisition Modes for Wetland Monitoring Applications. *Canadian Journal of Remote Sensing*, *41*(5), 431–439. https://doi.org/10.1080/07038992.2015.1104636

Brisco, B., Schmitt, A., Murnaghan, K., Kaya, S., & Roth, A. (2013). SAR polarimetric change detection for flooded vegetation. *International Journal of Digital Earth*, *6*(2), 103–114. https://doi.org/10.1080/17538947.2011.608813

Bridgham, S. D., Megonigal, J. P., Keller, J. K., Bliss, N. B., & Trettin, C. (2006). The carbon balance of North American wetlands. *Wetlands*, *26*(4), 28. https://doi.org/10.1672/0277-5212(2006)26[889:TCBONA]2.0.CO;2

Chapman, B., Siqueira, P., Saatchi, S., Simard, M., & Kellndorfer, J. (2019). Initial results from the 2019 NISAR Ecosystem Cal/Val Exercise in the SE USA. *IGARSS 2019 - 2019 IEEE International Geoscience and Remote Sensing Symposium*, 8641–8644. https://doi.org/10.1109/IGARSS.2019.8899227

Chen, Y., He, X., Wang, J., & Xiao, R. (2014). The Influence of Polarimetric Parameters and an Object-Based Approach on Land Cover Classification in Coastal Wetlands. *Remote Sensing*, *6*(12), 12575–12592. https://doi.org/10.3390/rs61212575

Choi, H., & Jeong, J. (2019). Speckle Noise Reduction Technique for SAR Images Using Statistical Characteristics of Speckle Noise and Discrete Wavelet Transform. *Remote Sensing*, *11*(10), 1184. https://doi.org/10.3390/rs11101184

591 Chuang, C.-L., Shaffer, S., Niamsuwan, N., Li, S., Vines, K., & Yang, M.-W. (2016). NISAR L-
592 band digital electronics subsystem: A multichannel system with distributed processors for
593 digital beam forming and mode dependent filtering. *2016 IEEE Radar Conference*
594 *(RadarConf)*, 1–5. https://doi.org/10.1109/RADAR.2016.7485225
595 Cloude, S. R., & Pottier, E. (1996). A review of target decomposition theorems in radar
596 polarimetry. *IEEE Transactions on Geoscience and Remote Sensing*, *34*(2), 498–518.
597 https://doi.org/10.1109/36.485127
598 Cloude, S. R., & Pottier, E. (1997). An entropy based classification scheme for land applications
599 of polarimetric SAR. *IEEE Transactions on Geoscience and Remote Sensing*, *35*(1), 68–
600 78. https://doi.org/10.1109/36.551935
601 Corcoran, J. M., Knight, J. F., & Gallant, A. L. (2013). Influence of Multi-Source and Multi-
602 Temporal Remotely Sensed and Ancillary Data on the Accuracy of Random Forest
603 Classification of Wetlands in Northern Minnesota. *Remote Sensing*, *5*(7), 3212–3238.
604 https://doi.org/10.3390/rs5073212
605 Cowardin, L. M., Carter, V., Golet, F. C., & LaRoe, E. T. (1979). *Classification of wetlands and*
606 *deepwater habitats of the United States* [Technical Report]. U.S. Department of the
607 Interior, U.S. Fish and Wildlife Service. https://tamug-ir.tdl.org/handle/1969.3/20139
608 Dahl, T. E., & Johnson, C. E. (1991). *Wetlands, Status and Trends in the Conterminous United*
609 *States, Mid-1970's to Mid-1980's: First Update of the National Wetlands Status Report*.
610 U.S. Department of the Interior, Fish and Wildlife Service.
611 Dahl, T. E. (n.d.). *Status and Trends of Wetlands in the Conterminous United States 2004 to*
612 *2009*. 112.
613 Duncanson, L., Neuenschwander, A., Hancock, S., Thomas, N., Fatoyinbo, T., Simard, M.,
614 Silva, C. A., Armston, J., Luthcke, S. B., Hofton, M., Kellner, J. R., & Dubayah, R.
615 (2020). Biomass estimation from simulated GEDI, ICESat-2 and NISAR across
616 environmental gradients in Sonoma County, California. *Remote Sensing of Environment*,
617 *242*, 111779. https://doi.org/10.1016/j.rse.2020.111779
618 Evans, T. L., & Costa, M. (2013). *Landcover classification of the Lower Nhecolândia subregion*
619 *of the Brazilian Pantanal Wetlands using ALOS/PALSAR, RADARSAT-2 and*
620 *ENVISAT/ASAR imagery*. https://pubag.nal.usda.gov/catalog/876316
621 Freeman, A., & Durden, S. L. (1998a). A three-component scattering model for polarimetric
622 SAR data. *IEEE Transactions on Geoscience and Remote Sensing*, *36*(3), 963–973.
623 https://doi.org/10.1109/36.673687
624 Freeman, A., & Durden, S. L. (1998b). A three-component scattering model for polarimetric
625 SAR data. *IEEE Transactions on Geoscience and Remote Sensing*, *36*(3), 963–973.
626 https://doi.org/10.1109/36.673687
627 Frohn, R. C., Autrey, B. C., Lane, C. R., & Reif, M. (2011). Segmentation and object-oriented
628 classification of wetlands in a karst Florida landscape using multi-season Landsat-7
629 ETM+ imagery. *International Journal of Remote Sensing*, *32*(5), 1471–1489.
630 https://doi.org/10.1080/01431160903559762
631 Furtado, L. F. de A., Silva, T. S. F., & Novo, E. M. L. de M. (2016). Dual-season and full-
632 polarimetric C band SAR assessment for vegetation mapping in the Amazon várzea
633 wetlands. *Remote Sensing of Environment*, *174*, 212–222.
634 https://doi.org/10.1016/j.rse.2015.12.013
635 Gardner, R. C., & Davidson, N. (2011). The Ramsar Convention. *Wetlands: Integrating*
636 *Multidisciplinary Concepts*, 189–203.

637 Hensley, S., Wheeler, K., Sadowy, G., Jones, C., Shaffer, S., Zebker, H., Miller, T., Heavey, B.,
638 Chuang, E., Chao, R., Vines, K., Nishimoto, K., Prater, J., Carrico, B., Chamberlain, N.,
639 Shimada, J., Simard, M., Chapman, B., Muellerschoen, R., … Smith, R. (2008). The
640 UAVSAR instrument: Description and first results. *2008 IEEE Radar Conference*, 1–6.
641 https://doi.org/10.1109/RADAR.2008.4720722
642 Hess, L. L., Melack, J. M., Affonso, A. G., Barbosa, C., Gastil-Buhl, M., & Novo, E. M. L. M.
643 (2015). Wetlands of the Lowland Amazon Basin: Extent, Vegetative Cover, and Dual-
644 season Inundated Area as Mapped with JERS-1 Synthetic Aperture Radar. *Wetlands*,
645 *35*(4), 745–756. https://doi.org/10.1007/s13157-015-0666-y
646 Hoffman, J. P., Horst, S., & Ghaemi, H. (2015). Digital calibration system for the proposed
647 NISAR (NASA/ISRO) mission. *2015 IEEE Aerospace Conference*, 1–7.
648 https://doi.org/10.1109/AERO.2015.7119151
649 Hong, S.-H., & Wdowinski, S. (2014). Multitemporal Multitrack Monitoring of Wetland Water
650 Levels in the Florida Everglades Using ALOS PALSAR Data With Interferometric
651 Processing. *IEEE Geoscience and Remote Sensing Letters*, *11*(8), 1355–1359.
652 https://doi.org/10.1109/LGRS.2013.2293492
653 Huang, Xiaodong, Michele Reba, Alisa Coffin, Benjamin R. K. Runkle, Yanbo Huang, Bruce
654 Chapman, Beth Ziniti, et al. 2021. “Cropland Mapping with L-Band UAVSAR and
655 Development of NISAR Products.” *Remote Sensing of Environment* 253 (February):
656 112180. https://doi.org/10.1016/j.rse.2020.112180.
657 Huynen, J. R. (1970). *Phenomenological theory of radar targets*.
658 Jaramillo, F., Brown, I., Castellazzi, P., Espinosa, L., Guittard, A., Hong, S.-H., Rivera-Monroy,
659 V. H., & Wdowinski, S. (2018). Assessment of hydrologic connectivity in an ungauged
660 wetland with InSAR observations. *Environmental Research Letters*, *13*(2), 024003.
661 https://doi.org/10.1088/1748-9326/aa9d23
662 Jong-Sen Lee, Jen-Hung Wen, Ainsworth, T. L., Kun-Shan Chen, & Chen, A. J. (2009).
663 Improved Sigma Filter for Speckle Filtering of SAR Imagery. *IEEE Transactions on*
664 *Geoscience and Remote Sensing*, *47*(1), 202–213.
665 https://doi.org/10.1109/TGRS.2008.2002881
666 Koch, M., Schmid, T., Reyes, M., & Gumuzzio, J. (2012). Evaluating Full Polarimetric C- and
667 L-Band Data for Mapping Wetland Conditions in a Semi-Arid Environment in Central
668 Spain. *IEEE Journal of Selected Topics in Applied Earth Observations and Remote*
669 *Sensing*, *5*(3), 1033–1044. https://doi.org/10.1109/JSTARS.2012.2202091
670 Krogager, E. (1990). New decomposition of the radar target scattering matrix. *Electronics*
671 *Letters*, *26*(18), 1525–1527. https://doi.org/10.1049/el:19900979
672 Li, D., & Zhang, Y. (2016). Unified Huynen Phenomenological Decomposition of Radar Targets
673 and Its Classification Applications. *IEEE Transactions on Geoscience and Remote*
674 *Sensing*, *54*(2), 723–743. https://doi.org/10.1109/TGRS.2015.2464113
675 Mahdianpari, M., Salehi, B., Mohammadimanesh, F., & Motagh, M. (2017). Random forest
676 wetland classification using ALOS-2 L-band, RADARSAT-2 C-band, and TerraSAR-X
677 imagery. *ISPRS Journal of Photogrammetry and Remote Sensing*, *130*, 13–31.
678 https://doi.org/10.1016/j.isprsjprs.2017.05.010
679 Martins, S., Bernardo, N., Ogashawara, I., & Alcantara, E. (2016). Support Vector Machine
680 algorithm optimal parameterization for change detection mapping in Funil Hydroelectric
681 Reservoir (Rio de Janeiro State, Brazil). *Modeling Earth Systems and Environment*, *2*(3),
682 138. https://doi.org/10.1007/s40808-016-0190-y

683 Millard, K., & Richardson, M. (2015). On the Importance of Training Data Sample Selection in
684 Random Forest Image Classification: A Case Study in Peatland Ecosystem Mapping.
685 *Remote Sensing*, *7*(7), 8489–8515. https://doi.org/10.3390/rs70708489
686 Mitsch, W. J., Bernal, B., Nahlik, A. M., Mander, Ü., Zhang, L., Anderson, C. J., Jørgensen, S.
687 E., & Brix, H. (2013). Wetlands, carbon, and climate change. *Landscape Ecology*, *28*(4),
688 583–597. https://doi.org/10.1007/s10980-012-9758-8
689 Mohammadimanesh, F., Salehi, B., Mahdianpari, M., Brisco, B., & Gill, E. (2019). Full and
690 Simulated Compact Polarimetry SAR Responses to Canadian Wetlands: Separability
691 Analysis and Classification. *Remote Sensing*, *11*(5), 516.
692 https://doi.org/10.3390/rs11050516
693 Mohammadimanesh, F., Salehi, B., Mahdianpari, M., Brisco, B., & Motagh, M. (2018). Multi-
694 temporal, multi-frequency, and multi-polarization coherence and SAR backscatter
695 analysis of wetlands. *ISPRS Journal of Photogrammetry and Remote Sensing*, *142*, 78–
696 93. https://doi.org/10.1016/j.isprsjprs.2018.05.009
697 Mountrakis, G., Im, J., & Ogole, C. (2011). Support vector machines in remote sensing: A
698 review. *ISPRS Journal of Photogrammetry and Remote Sensing*, *66*(3), 247–259.
699 https://doi.org/10.1016/j.isprsjprs.2010.11.001
700 Pal, M. (2005). Random forest classifier for remote sensing classification. *International Journal*
701 *of Remote Sensing*, *26*(1), 217–222. https://doi.org/10.1080/01431160412331269698
702 *Simulated NISAR Products*. (2020). https://uavsar.jpl.nasa.gov/science/documents/nisar-sample-
703 products.html
704 Pistolesi, L. I., Ni-Meister, W., & McDonald, K. C. (2015). Mapping wetlands in the Hudson
705 Highlands ecoregion with ALOS PALSAR: An effort to identify potential swamp forest
706 habitat for golden-winged warblers. *Wetlands Ecology and Management*, *23*(1), 95–112.
707 https://doi.org/10.1007/s11273-014-9381-3
708 Qi, Z., Yeh, A. G.-O., Li, X., & Lin, Z. (2012). A novel algorithm for land use and land cover
709 classification using RADARSAT-2 polarimetric SAR data. *Remote Sensing of*
710 *Environment*, *118*, 21–39. https://doi.org/10.1016/j.rse.2011.11.001
711 Rodriguez-Galiano, V. F., Ghimire, B., Rogan, J., Chica-Olmo, M., & Rigol-Sanchez, J. P.
712 (2012). An assessment of the effectiveness of a random forest classifier for land-cover
713 classification. *ISPRS Journal of Photogrammetry and Remote Sensing*, *67*, 93–104.
714 https://doi.org/10.1016/j.isprsjprs.2011.11.002
715 Salehi, B., Daneshfar, B., & Davidson, A. M. (2017). Accurate crop-type classification using
716 multi-temporal optical and multi-polarization SAR data in an object-based image analysis
717 framework. *International Journal of Remote Sensing*, *38*(14), 4130–4155.
718 Salehi, Bahram, Mahdianpari, M., Amani, M., M.Manesh, F., Granger, J., Mahdavi, S., &
719 Brisco, B. (2018). A Collection of Novel Algorithms for Wetland Classification with
720 SAR and Optical Data. *Wetlands Management - Assessing Risk and Sustainable*
721 *Solutions*. https://doi.org/10.5772/intechopen.80688
722 Sheykhmousa, M., & Mahdianpari, M. (2020). Support Vector Machine vs. Random Forest for
723 Remote Sensing Image Classification: A Meta-analysis and systematic review. *IEEE*
724 *Journal of Selected Topics in Applied Earth Observations and Remote Sensing*.
725 https://doi.org/10.1109/JSTARS.2020.3026724
726 Singh, G., Yamaguchi, Y., & Park, S.-E. (2013). General Four-Component Scattering Power
727 Decomposition With Unitary Transformation of Coherency Matrix. *IEEE Transactions*

on Geoscience and Remote Sensing, *51*(5), 3014–3022. https://doi.org/10.1109/TGRS.2012.2212446

Stedman, S.-M., & Dahl, T. E. (n.d.). *Status and Trends of Wetlands in the Coastal Watersheds of the Eastern United States 1998 to 2004*. 36.

Tao, W., Jin, H., & Zhang, Y. (2007). Color Image Segmentation Based on Mean Shift and Normalized Cuts. *IEEE Transactions on Systems, Man, and Cybernetics, Part B (Cybernetics)*, *37*(5), 1382–1389. https://doi.org/10.1109/TSMCB.2007.902249

Thanh Noi, P., & Kappas, M. (2018). Comparison of Random Forest, k-Nearest Neighbor, and Support Vector Machine Classifiers for Land Cover Classification Using Sentinel-2 Imagery. *Sensors*, *18*(1), 18. https://doi.org/10.3390/s18010018

Tian, S., Zhang, X., Tian, J., & Sun, Q. (2016). Random Forest Classification of Wetland Landcovers from Multi-Sensor Data in the Arid Region of Xinjiang, China. *Remote Sensing*, *8*(11), 954. https://doi.org/10.3390/rs8110954

Tiner, R. W., Lang, M. W., Klemas, V. V., Lang, M. W., & Klemas, V. V. (2015). *Remote Sensing of Wetlands: Applications and Advances*. CRC Press. https://doi.org/10.1201/b18210

Touzi, R. (2007). Target Scattering Decomposition in Terms of Roll-Invariant Target Parameters. *IEEE Transactions on Geoscience and Remote Sensing*, *45*(1), 73–84. https://doi.org/10.1109/TGRS.2006.886176

Touzi, R. (2010). *INTERPRETATION OF THE TOUZI DECOMPOSITION FOR OPTIMUM WETLAND CHARACTERIZATION*. 4.

Tsyganskaya, V., Martinis, S., Marzahn, P., & Ludwig, R. (2018). SAR-based detection of flooded vegetation – a review of characteristics and approaches. *International Journal of Remote Sensing*, *39*(8), 2255–2293. https://doi.org/10.1080/01431161.2017.1420938

Wang, W., Tian, Z., Tian, B., & Zhang, J. (2020). Supervised Manifold-Learning Algorithm for Polsar Feature Extraction and Lulc Classification. *The International Archives of Photogrammetry, Remote Sensing and Spatial Information Sciences; Gottingen*, *XLIII-B3-2020*, 345–350. http://dx.doi.org/10.5194/isprs-archives-XLIII-B3-2020-345-2020

Wohlfart, C., Winkler, K., Wendleder, A., & Roth, A. (2018). TerraSAR-X and Wetlands: A Review. *Remote Sensing*, *10*(6), 916. https://doi.org/10.3390/rs10060916

Yu, Y., & Saatchi, S. (2016). Sensitivity of L-Band SAR Backscatter to Aboveground Biomass of Global Forests. *Remote Sensing*, *8*(6), 522. https://doi.org/10.3390/rs8060522

Yucatan Lake Topo Map in Tensas Parish, Louisiana. (n.d.). Retrieved July 21, 2020, from https://www.anyplaceamerica.com/directory/la/tensas-parish-22107/lakes/yucatan-lake-556489/

Zhao, J., Niu, Y., Lu, Z., Yang, J., Li, P., & Liu, W. (2018). Applicability Assessment of Uavsar Data in Wetland Monitoring: A Case Study of Louisiana Wetland. *ISPRS - International Archives of the Photogrammetry, Remote Sensing and Spatial Information Sciences*, *42.3*, 2375–2378. https://doi.org/10.5194/isprs-archives-XLII-3-2375-2018

Zhu, G., & Blumberg, D. G. (2002). Classification using ASTER data and SVM algorithms;: The case study of Beer Sheva, Israel. *Remote Sensing of Environment*, *80*(2), 233–240. https://doi.org/10.1016/S0034-4257(01)00305-4